nature communications

Article

https://doi.org/10.1038/s41467-025-67094-9

Probing electrical double layer via triboelectric charge transfer

Received: 12 June 2025

Accepted: 19 November 2025

Published online: 07 December 2025

Check for updates

A list of authors and their affiliations appears at the end of the paper

The nanoscale electrical double layer (EDL) governs macroscopic phenomena such as ion adsorption and reaction kinetics, serving as a fundamental determinant in diverse applications ranging from sensing, and catalysis, to energy storage. While classical EDL models primarily describe conductive interfaces, most naturally occurring EDLs form at non-conductive surfaces in liquid environment, where characterization remains fundamentally challenging due to the constraints of conventional techniques. Here, we present a triboelectric nanogenerator (TENG)-based triboelectric charge transfer probe that utilizes the intrinsic solid-liquid contact electrification (CE) process to operando monitor the formation and evolution of the EDL at non-conductive interfaces. This bias-free and electrode-independent approach enables direct probing of interfacial charge dynamics fundamentally inaccessible to conventional electrochemical approaches constrained by conductive substrate dependencies and external potential requirements. This method also reveals distinct EDL behaviors, particularly in electrolytes with asymmetric ion sizes at concentrations exceeding 10^{-1} M and at non-conductive interfaces. Its fundamental mechanism and measurement precision were rigorously validated via atomic force microscopy, Kelvin probe force microscopy, surface-enhanced Raman spectroscopy, and molecular dynamics simulations, establishing a robust analytical platform and theoretical basis for EDL studies. This work introduces a CE-based methodology for direct triboelectric charge characterization on dielectric surfaces, overcoming conventional conductive substrate limitations. By integrating classical EDL theory with triboelectric frameworks, we establish models resolving interfacial charge dynamics across diverse solid-liquid interfaces, including high ionic strength regimes. It confirms material-agnostic applicability. This paradigm simultaneously advances fundamental EDL mechanisms and enables programmable charge manipulation for next-generation iontronic power, sensing, and neuromorphic devices.

The electrical double layer (EDL)[1], formed at solid-liquid or liquid-liquid interfaces, etc., is fundamental to energy storage[2,3], catalysis[4], and colloidal stability[5], critically affecting reaction kinetics[6], corrosion resistance[7], sensor performance[8], and device efficiency across disciplines. The concept was first introduced by Hermann von Helmholtz in the 19th century[9], who proposed that charges on a metal surface are compensated by a compact layer of counterions. While foundational, this model is overly idealized, neglecting ion mobility and solvent effects, and cannot accurately describe charge distribution or potential variation at real interfaces. In the early 20th century, Gouy and

e-mail: zqtian@xmu.edu.cn; zlwang@binn.cas.cn; weidi@binn.cas.cn

Chapman independently extended this view by introducing a diffuse ion layer governed by electrostatic forces and thermal fluctuations, leading to the Gouy-Chapman model[10]. This framework captures the exponential decay of ion concentration with distance from the surface but treats ions as point charges, ignoring their finite size, hydration shells, and specific adsorption. To overcome these limitations, Stern proposed the Gouy-Chapman-Stern (GCS) model in 1924[11], combining Helmholtz's compact layer and Gouy-Chapman's diffuse layer. The GCS model partitions the interface into the inner Helmholtz plane (IHP), comprising the charged electrode surface and specifically adsorbed ions, and the outer Helmholtz plane (OHP), consisting of solvated ions, together forming the Stern layer, beyond which the diffuse layer extends into the bulk. At low electrolyte concentrations, this model effectively captures ion distribution and dynamics near charged interfaces. While classical EDL theory has traditionally been applied to conductive interfaces, recent studies demonstrate that dielectric materials can also sustain EDL formation[5,12,13]. Nevertheless, conventional models are inadequate for non-conductive solid interfaces, owing to experimental limitations in directly probing EDL structure. Their applicability further diminishes at high ionic strengths ($>10^{-1}$ M), where interfacial ion correlations[14], steric exclusion effects[15], and specific adsorption energetics dominate interfacial reorganization. Moreover, the model neglects solvent structuring, non-local dielectric responses, and interfacial dynamics such as polarization and specific ion adsorption. These limitations become especially evident in systems exhibiting charge inversion, a nontrivial phenomenon in which accumulated counterions exceed what is required to neutralize the surface charge. Charge inversion arises from a complex interplay of ion asymmetry[16], hydrophilicity[17], hydrophobicity[18,19], and surface charge density[20,21], especially with asymmetric ions (in size, valency, or polarizability) enhancing correlations that promote overcompensation. Despite growing experimental and simulation-based evidence, the molecular-scale mechanisms underlying such behaviors remain incompletely understood. These challenges underscore the need for advanced theoretical models and interface-sensitive measurement techniques capable of capturing the full complexity of EDL structures at non-conductive surfaces and under high ionic strength.

The EDL, a fundamental interfacial structure governing charge transfer and electrochemical dynamics, has been explored through a wide range of experimental techniques. For conductive interfaces[22,23], methods such as electrochemical impedance spectroscopy (EIS), cyclic voltammetry, and scanning electrochemical microscopy (SECM) offer sensitivity to potential-dependent ion redistribution. However, they are limited by electrode polarization and substrate requirements, particularly at high electrolyte concentrations, where interfacial reactions may occur. A range of advanced techniques has also been developed to investigate the structural characteristics of EDL, each with distinct advantages and limitations. Optical spectroscopic methods, such as in situ Raman spectroscopy[24], surface-enhanced Raman spectroscopy (SERS)[25,26], and infrared spectroscopy[27], are widely used for their molecular sensitivity. In situ Raman spectroscopy enables non-destructive analysis but suffers from low sensitivity and fluorescence interference. SERS significantly enhances signal intensity, allowing the detection of trace species, yet it relies on carefully engineered plasmonic substrates, involves high fabrication costs, and presents challenges in spectral interpretation. Infrared spectroscopy offers molecular fingerprinting capabilities but is hindered by strong water absorption and poor suitability for real-time studies. Atomic force microscopy (AFM)-based techniques[28], such as Kelvin probe force microscopy (KPFM), allow direct probing of interfacial potential and dielectric properties under realistic electrolyte conditions with nanoscale resolution. However, KPFM measurements are strongly influenced by tip geometry, long-range electrostatic coupling, and the dielectric environment. While KPFM measures surface potential/work function on insulators, charge accumulation and slower dissipation on insulating surfaces cause lower signal-to-noise ratios and susceptibility to charge injection interference, posing greater challenges than conductor/semiconductor measurements. Additionally, it only provides potential information rather than direct charge transfer measurements and extracting surface charge requires complex modeling and calibration. Quartz crystal microbalance (QCM) offers high sensitivity to mass changes and is valuable for tracking EDL dynamics, but it typically requires conductive or specially coated substrates and stringent control over experimental conditions[29]. X-ray-based methods provide atomically resolved information on the arrangement of ions and molecules at interfaces, making them powerful tools for the structural analysis of EDL[30]. Nonetheless, they struggle with detecting liquid, especially in aqueous or complex environments, and their reliance on specialized, expensive equipment further limits accessibility. Theoretical computational methods offer atomic-level insights into EDL formation and ion distribution but often fall short of capturing the complexity of real interfacial systems, resulting in discrepancies with experimental observations. Therefore, despite the wide array of available techniques, a reliable and straightforward testing method capable of probing EDL structures at non-conductive interfaces, particularly under high-concentration electrolyte conditions, remains elusive. Conventional techniques are often ineffective at probing these interfaces, necessitating alternative approaches.

Contact electrification (CE), one of the oldest documented physical phenomena[31], is traditionally regarded as a surface charge transfer between dissimilar materials upon contact and separation. However, it has recently undergone a scientific resurgence. Far from being fully resolved, CE has re-emerged as a rich platform for exploring fundamental interfacial processes at the molecular scale. Recent findings demonstrate that contact-induced charge transfer can also occur between identical insulators, giving rise to spontaneous long-range electrostatic ordering[32]. Investigations at oil-water interfaces reveal that the electric fields originate directly from the contact between the water and oil interface[33]. Collectively, these advances reposition charge transfer based on CE as a contemporary frontier in interfacial science, bridging solid-solid and liquid-liquid interfaces while offering mechanistic insights into the origins of interfacial charge, dielectric asymmetry, and electrostatic ordering in complex environments. Notably, charge transfer based on CE is particularly prominent at solid-liquid interfaces, where dielectric solids interact with liquids to produce intricate interfacial phenomena[34–37]. Solid-liquid triboelectric nanogenerators (TENGs) based on CE have also emerged as highly sensitive probes for detecting charge transfer between droplets and dielectric surfaces[36–39], and for capturing rapid interfacial dynamics, such as those observed in the Leidenfrost effect[40], thereby enabling real-time insights into charge evolution at dynamic interfaces. At these interfaces, the solid surface engages in intricate interactions with ions and molecules in the liquid phase, initiating processes including electron transfer, ion exchange, and EDL formation. Recent studies have proposed a "two-step" EDL model[12] extending the GCS framework to dielectric solid-liquid interfaces. First, contact between a dielectric solid and water induces electronic polarization through electron cloud overlap and hydrogen-bonding interactions, while surface groups undergo partial ionization to generate localized fixed charges. This defines the IHP, comprising the charged solid surface and specifically adsorbed ions. In the second stage, ions in the liquid redistribute to compensate for these charges, forming the OHP. The IHP and OHP together form the Stern layer, a compact region where most of the interfacial potential drop occurs. Beyond it, the diffuse layer exhibits a gradual transition to bulk concentration and remains more sensitive to external conditions. The EDL as a whole dictates the fundamental properties of the solid-liquid interface. Unlike conductor-based models, where mobile surface electrons sustain the EDL under applied voltage, dielectric systems rely on an electrostatically asymmetric and partially immobile polarization

layer. The two-step model has since been widely applied across diverse contexts and provides a foundation for triboiontronics, enabling dynamic reconfiguration of dielectric-liquid EDLs via triboelectric field modulation and precise control of ion transport kinetics[41–43]. This strategy unlocks new possibilities for high-efficiency energy scavenging, neuromorphic ionic logic, and self-powered information systems. Despite significant progress, EDL behavior in high-concentration and asymmetric electrolyte systems remains largely unexplored, representing a critical gap in current understanding. Moreover, the lack of effective probing methods for EDLs on non-conductive surfaces has hindered deeper insights into interfacial charge dynamics. Addressing these challenges is of fundamental importance for deciphering the diverse charge signatures observed across electrolytes during CE and for unveiling the dynamic evolution of EDLs at solid-liquid interfaces. Utilizing triboelectric charge measurement with a TENG, offering direct access to CE-induced charge, provides a promising platform for the investigation of EDL formation on dielectric surfaces. Such approaches hold immense potential for advancing interfacial iontronic charge regulation, with far-reaching implications in various applications.

In this study, a disruptive alternative is presented that harnesses TENG as a straightforward operando probe to elucidate the formation and evolution of EDLs across a wide range of electrolyte concentrations. Unlike conventional methods requiring conductive interfaces and external bias, this TENG-based triboelectric charge transfer probe enables bias-free, straightforward testing of interfacial charge density on non-conductive surfaces, effectively circumventing Faradaic interference and preserving the native EDL structure. It reveals the diverse static EDL architectures formed by various electrolytes, including under high ionic strength conditions and at the non-conductive interfaces. It confirms material-agnostic applicability. KPFM, SERS, and molecular dynamics (MD) simulations are integrated as validation tools to confirm the accuracy of the triboelectric charge probe and to provide complementary spectroscopic and atomistic insights. Collectively, these advances establish TENG-based triboelectric charge transfer probing as a substrate-agnostic platform for interfacial iontronic investigations. Its non-perturbative nature enables zero-bias interrogation of native EDL structures, even in dynamic systems like high-flow-rate electrolytes, while revealing fundamental insights into EDL. This paradigm simultaneously advances fundamental EDL mechanisms and enables programmable charge manipulation for next-generation iontronic power, sensing, and neuromorphic devices.

Results

Probing EDL based on triboelectric charge transfer

In the CE process, the electron-cloud-potential-well model has been widely employed to describe charge transfer driven by electron cloud interactions. Within this framework, atoms or molecules are depicted as potential wells that spatially confine delocalized electron clouds. Each atom is modeled as a potential well wherein valence electrons are weakly bound, collectively constituting the atomic or molecular electron cloud. As shown in Fig. 1a, d denoted the distance between electron clouds. Before contact, electrons were trapped within these wells, preventing inter-material transfer. Upon contact between water molecules and a dielectric surface, screening-induced electron cloud overlap transforms the initially symmetric potential wells into asymmetric double-well configurations. This asymmetry facilitates the quantum tunneling of electrons from the water molecules to the solid surface, thereby initiating charge transfer. As illustrated in Fig. 1b, thermal motion and interfacial pressure drive water molecules and solvated ions, primarily H_2O, cations, and anions, into dynamic collisions with the solid interface. These collisions induce electron transfer through electron cloud overlaps, alongside interfacial ionization reactions. The dielectric solid undergoes electronic polarization and partial ionization of surface groups, generating localized charges that form the IHP with specifically adsorbed ions. Liquid ions then redistribute to form the OHP, together constituting the Stern layer where most of the interfacial potential drop occurs. Beyond this, the diffuse layer extended into the bulk solution, completing the EDL structure. The TENG-based triboelectric charge transfer detection setup comprises a PTFE film for CE and a copper layer functioning as the induction electrode (Fig. 1c). When deionized (DI) water contacted the solid surface, CE-induced electron transfer occurred with the self-ionization of water, generating ions that participated in interfacial ion exchange. Following electron transfer, ions were adsorbed onto the surface, further promoting interfacial ion accumulation. This combined transfer of electrons and ions imparted a net negative charge to the solid surface, which subsequently attracted counterions from the liquid, culminating in EDL formation at the solid-liquid interface.

Upon the introduction of an electrolyte, the EDL underwent further modulation through complex interactions between the added cations and anions and the pre-existing interfacial environment. These ions reshaped the interfacial charge distribution, electrostatic potential, and ionic composition, with outcomes strongly governed by ion-specific parameters such as size, valency, and hydration characteristics. Together, these factors defined the structural and dynamic properties of evolving EDL. For symmetric electrolytes such as LiCl solution, charge transfer gradually decreased with increasing concentration and plateaued upon reaching a critical concentration (Fig. 1d and S1). LiCl dissociated into Li^+ and Cl^- in water, increasing the population of free ions available for EDL formation at the solid-liquid interface. Rising ionic concentration promoted the development of a more compact EDL due to the elevated ion density. Once a more compact EDL formed in LiCl, it effectively attenuated electron transfer, reducing the charge output during CE[13]. In contrast, asymmetric electrolytes introduced additional complexity. Prior studies have reported charge inversion[44,45] in systems with ion size, valence, or polarizability disparities, where disrupted ion-ion correlations within the EDL could lead to local overcompensation of surface charge and even net charge reversal. However, the mechanisms by which ionic asymmetric modulated EDL structure remain poorly understood. In this study, EDL behavior in high-concentration asymmetric electrolytes was investigated to address this gap. Li[TFSI], characterized by its combination of bulky anions and small cations, represented a prototypical asymmetric electrolyte system to elucidate the impact of ionic asymmetric (Figure. S2a). To assess the impact of EDL formation dynamics under such ionic asymmetry, Li[TFSI] was investigated using the same TENG-basedtriboelectric charge measurements. At an initial concentration of 10^{-3} M, the transferred charge was positive. As the concentration increased to 10^{-2} M, the charge transfer decreased but remained positive. However, upon further increasing the concentration to 10^{-1} M, the transferred charge inverted, becoming negative, a signature of altered EDL formation dynamics. This negative charge transfer persisted at 1 M, indicating a concentration-dependent transition in interfacial charge behavior driven by the asymmetric nature of the electrolyte (Fig. 1e, S3). [EMIM]Cl, an electrolyte featuring large-sized cations and smaller anions (Figure. S2b), was selected to further examine EDL formation and dynamics in high-concentration asymmetric systems. The transferred charge was also observed to be initially positive at low concentrations. However, as the concentration increased, the charge transferred progressively declined and ultimately inverted to negative, reflecting a distinct ion-specific EDL formation mechanism driven by the asymmetric ion sizes (Fig. 1f, S4). It should also be noted that triboelectric charge measurements utilizing TENG on solid LiCl, Li[TFSI], and [EMIM]Cl revealed charge polarities consistent with the direction of charge transfer observed in their respective high-concentration solutions (Figure. S5, S6, and S7).

To verify the correlation between electrolyte-dependent electrical outputs and distinct EDL formation mechanisms in CE, the triboelectric charge transfer behaviors of LiCl, Li[TFSI], and [EMIM]Cl

https://doi.org/10.1038/s41467-025-67094-9

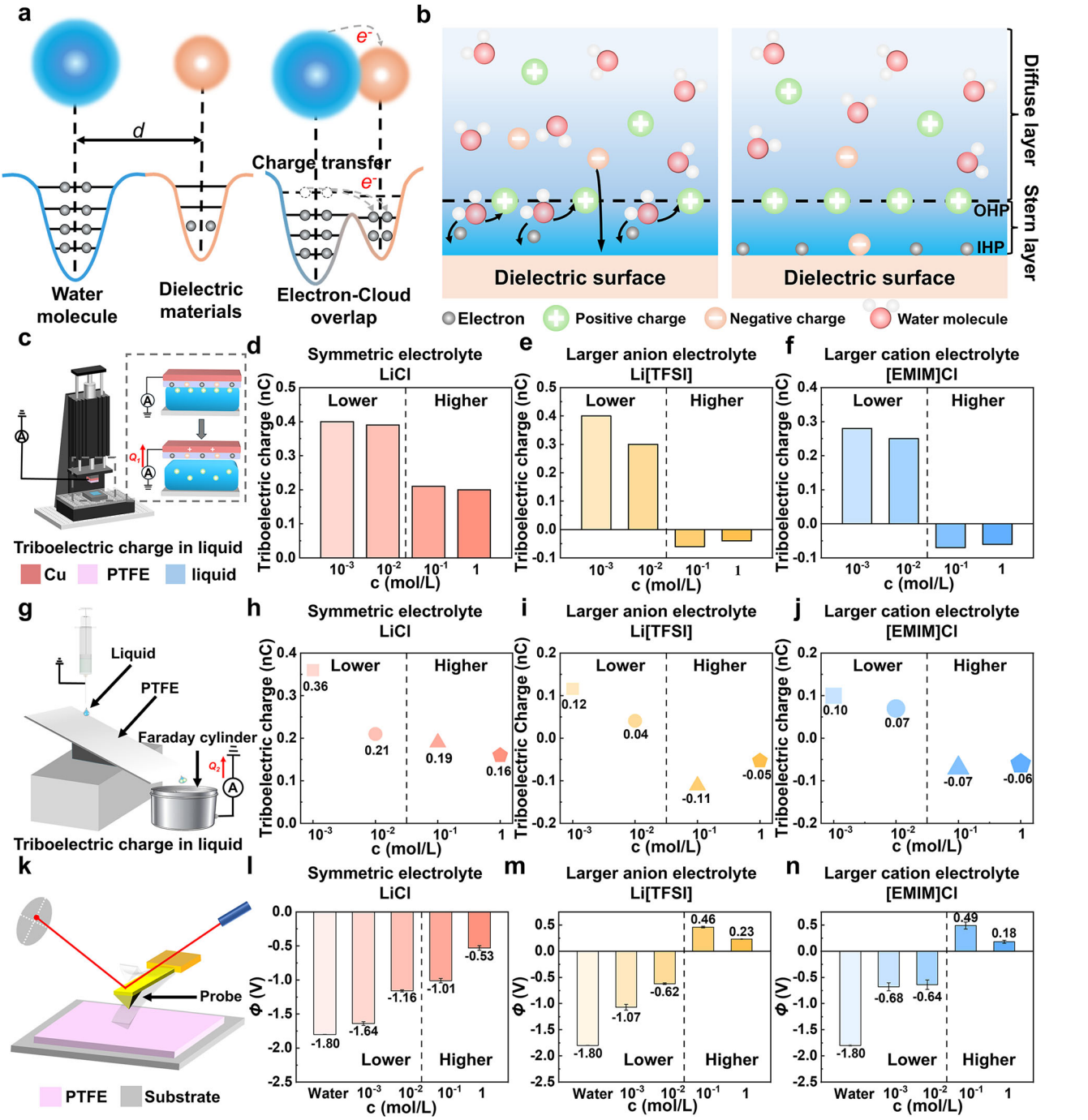

Fig. 1 | The mechanism of electrical double layer (EDL) formation induced by contact electrification (CE) and transferred charge at the solid–liquid (S-L) interface of different electrolytes. a Schematic illustration of the electron-cloud-potential-well model. **b** Two-step model of EDL formation induced by CE. (Inner Helmholtz Plane (IHP), Outer Helmholtz Plane (OHP)) **c** Schematic of the triboelectric nanogenerator (TENG) for triboelectric charge transfer measurement facilities. **d** The transferred charge during CE between different concentrations of LiCl solution and PTFE. **e** The transferred charge during CE between different concentrations of Li[TFSI] solution and PTFE. **f** The transferred charge during CE between different concentrations of [EMIM]Cl solution and PTFE. **g** Schematic of the Faraday cylinder testing apparatus. **h** The transferred charge by droplets of LiCl solution passing over the PTFE film at different concentrations. **i** The transferred charge by droplets of Li[TFSI] solution passing over the PTFE film at different concentrations. **j** The transferred charge by droplets of [EMIM]Cl solution passing over the PTFE film at different concentrations. **k** Schematic of the Kelvin probe force microscopy (KPFM) setup for measuring surface potential. **l** Surface potential of PTFE during CE with LiCl solution at different concentrations. **m** Surface potential of PTFE during CE with Li[TFSI] solution at different concentrations. **n** Surface potential of PTFE during CE with [EMIM]Cl solution at different concentrations.

solutions were systematically characterized under varying experimental conditions (Fig. 1g). The PTFE film was installed at a 45° incline, and a grounded syringe was used to continuously release a droplet of ~25 μL of solution onto the film. When the droplet slid across the PTFE film into the Faraday cylinder, the triboelectric charge carried by the droplet was measured. When LiCl solution was used, the droplet-transferred charge progressively decreased with increasing concentration (Fig. 1h, S8), as the formation of a more compact EDL enhanced charge screening and suppressed electron transfer. In the case of Li[TFSI], a similar trend was observed at lower concentrations,

with the transferred charge decreasing as the EDL became compact. When the concentration exceeded 10^{-1} M, changes in the formation mechanism of the EDL led to a reversal of the transferred charge from positive to negative (Fig. 1i, S9). A comparable inversion was also found in [EMIM]Cl solutions, where low-concentration measurements yielded positive charge transfer, followed by a polarity reversal at higher concentrations (Fig. 1j, S10). To further investigate interfacial charge behavior, each electrolyte solution was brought into contact with the PTFE surface and then dried, after which the surface potential of the PTFE was measured using KPFM. The resulting surface potential reflected the net transferred charge during the CE process (Fig. 1k). Initially, the surface potential of the PTFE film after CE with DI water was −1.80 V. When CE was conducted using LiCl solutions of increasing concentration, the surface potential rose from −1.64 V at 10^{-3} M to −0.53 V at 1 M while remaining consistently negative. This indicates that the liquid phase generated positive charges, and the PTFE film acquired negative charges throughout the process (Fig. 1l). When Li[TFSI] solutions of varying concentrations were used, the surface potential remained negative at 10^{-3} M and 10^{-2} M (~ −1 V to −0.6 V) but reversed to positive at 10^{-1} M and 1 M (~ 0.4 V to 0.2 V) (Fig. 1m), indicating that Li[TFSI] generated positive charges during CE at low concentrations, while producing negative charges at higher concentrations. A similar trend was observed for [EMIM]Cl solutions: the surface potential was negative at 10^{-3} M and 10^{-2} M (~ −0.6 V) but became positive as the concentration increased to 10^{-1} M and 1 M (~ 0.4 V to 0.2 V) (Fig. 1n). These results, consistent across KPFM, TENG, and Faraday cylinder measurements, confirm asymmetric electrolytes drive charge inversion in CE. By analyzing the triboelectric output signals, the dynamic evolution of the EDL might be revealed. These TENG-based triboelectric charge transfer measurements offer a powerful, multifunctional probe for in situ characterization of EDL formation and interfacial charge behaviors at solid-liquid interfaces.

Charge inversion may stem from factors such as ionic asymmetry, hydrophobicity, and surface charge density. Asymmetric ions intensify ion-ion correlations within the EDL, enabling charge overcompensation. Hydrophobic ions tend to adsorb at interfaces, while high surface charge densities enhance counterion accumulation. Although these phenomena are supported by both experiments and simulations, their molecular origins remain poorly understood due to the complex interplay of ionic interactions and interfacial dynamics. Importantly, the ability to harness charge inversion offers powerful means for manipulating interfacial charge behavior in advanced iontronic systems. For instance, charge reversal in polyelectrolyte-confined fluid memristors[19,44,45] enables precise control of ionic dynamics, effectively bridging chemical and electrical signals, a key mechanism underpinning the development of bio-inspired neuromorphic computing architectures. In biological neural networks, chemical stimuli often trigger electrical responses, with charge reversal serving as the fundamental physical basis for this transduction. By regulating charge reversal behavior, the accumulation and dissipation of ions in nanoscale channels can be effectively controlled, allowing for the emulation and control of synaptic-like memory behaviors. Controlled ionic charge inversion in a polyelectrolyte-confined fluidic memristor could enable bio-inspired neuromorphic computing, bridging chemical and electrical signaling for next-generation adaptive neuroprosthetics and brain-machine interfaces.

Investigating the formation of EDL in asymmetric electrolytes

To further investigate the mechanism behind charge inversion in asymmetric electrolytes during the CE process and to elucidate the formation of the EDL, a combined approach involving experimental measurements and MD simulations was employed. This integrated analysis aimed to enhance the accuracy and reliability of the triboelectric charge transfer probe for studying EDL formation in detail. The conductivity of each solution at various concentrations was measured using a conductivity meter, showing a gradual increase in conductivity with increasing concentration (Figure. S11a). The ion mobility was calculated using the Nernst-Einstein equation[46], and the relationship between ion mobility (u) and ionic conductivity (K) can be expressed by the following equation:

$$u = \frac{K}{c \cdot |z| \cdot F} \tag{1}$$

where c is the ion concentration, z is the ion charge, and F is the Faraday constant. The ion mobility of LiCl and [EMIM]Cl gradually decreased with increasing concentration. However, in the case of Li[TFSI], the ion mobility initially increased as the concentration rose from 10^{-3} M to 10^{-2} M, but it began to decrease as the concentration continued to increase (Figure. S11b). The relationship between diffusion coefficient (D) and ion mobility (u) can be expressed by the following equation:

$$D = u \cdot \frac{K_B \cdot N_A \cdot T}{|z| \cdot e \cdot N_A} = u \cdot \frac{R \cdot T}{|z| \cdot F} \tag{2}$$

where K_B is the Boltzmann constant, N_A is the Avogadro constant, T is the absolute temperature, e is the elementary charge, and R is the gas constant. The diffusion coefficient of LiCl and [EMIM]Cl decreased with an increase in concentration, while the diffusion coefficient of Li[TFSI] initially increased and then decreased, remaining consistently smaller than that of LiCl at the same concentration (Figure. S12). Since the ion conductivity meter provides only the overall diffusion coefficient of the electrolyte and cannot resolve the mobility of individual ionic species, MD simulations were employed to calculate the diffusion coefficients of individual ions in detail. The composition and configuration of the simulation boxes used for these calculations are summarized in Table S1. By adding different amounts of Li^+ and Cl^- in the same system to achieve the concentrations used in the experiments (Fig. S13). However, as the concentration continued to increase, the diffusion coefficients exhibited changes, with Cl^- consistently exhibiting a higher diffusion coefficient than Li^+ regardless of the concentration (Fig. 2a, S14 and Supplementary Data 1-4). During the CE process, electron transfer occurs first, followed by the adsorption of Cl^- onto the PTFE surface, which imparts a net negative charge to the PTFE and establishes the IHP of the EDL. Due to the high hydration-free energy of Li^+, it typically could not escape from its hydration shell to enter the dipole layer of water molecules and thus could not directly enter the IHP. As a result, the hydrated Li^+ ions formed the OHP, completing the EDL structure (Fig. 2b, c). This EDL formation inhibited electron transfer, thereby reducing the amount of transferred charge. As concentration increased, the higher ionic strength led to a denser EDL, suppressing electron transfer. However, in the case of LiCl, the overall charge remained negative across all concentrations. To replicate the experimental conditions in simulations, varying amounts of Li^+ and $[TFSI]^-$ were introduced into the same system to construct the corresponding electrolyte concentrations (Figure. S15). Notably, a distinct deviation from the behavior observed in LiCl solutions was found: at lower concentrations (10^{-3} M to 10^{-2} M), the diffusion coefficient of $[TFSI]^-$ exceeded that of Li^+, whereas at higher concentrations (10^{-1} M and 1 M), $[TFSI]^-$ exhibited a lower diffusion coefficient than Li^+, highlighting a concentration-dependent reversal in ionic mobility likely driven by the increasing steric hindrance and aggregation tendencies of bulky $[TFSI]^-$ (Fig. 2d, S16 and Supplementary Data 5-8). During the formation of the EDL, anions are generally more prone to specific adsorption than cations. At concentrations between 10^{-3} M and 10^{-2} M, the migration speed of $[TFSI]^-$ was higher than that of Li^+, resulting in an EDL formation process like that observed with LiCl (Fig. 2e). However, when the concentration exceeded 10^{-1} M, $[TFSI]^-$ diffusion slowed significantly due to steric

https://doi.org/10.1038/s41467-025-67094-9

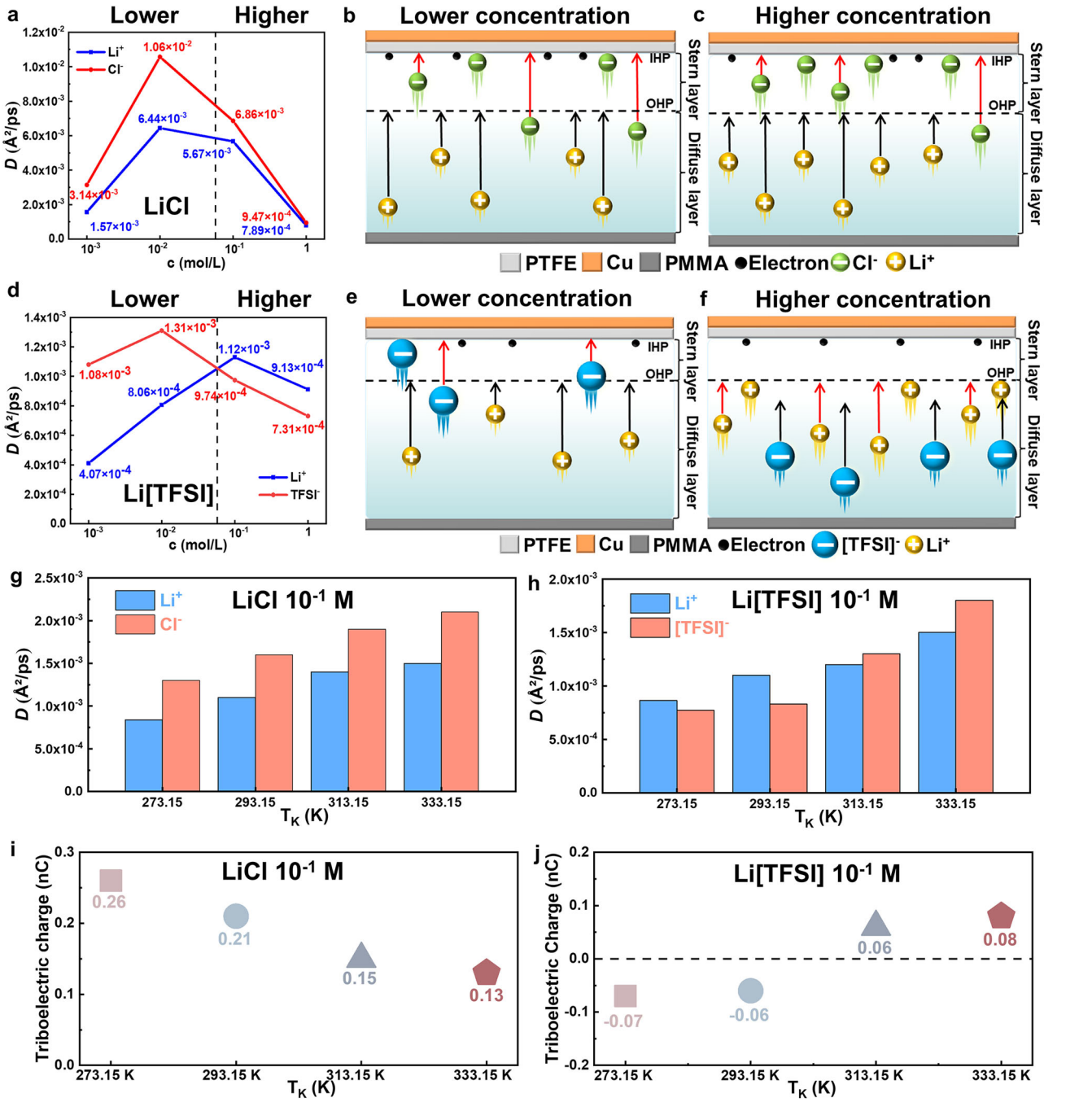

Fig. 2 | Molecular dynamics (MD) simulations of LiCl and Li[TFSI] at different concentrations and temperatures, along with tests at various temperatures. **a** Diffusion coefficient of Li^+ and Cl^- at various concentrations. **b** Electrical double layer (EDL) model of LiCl solution at a lower concentration. (inner Helmholtz plane (IHP), outer Helmholtz plane (OHP)) **c** EDL model of LiCl solution at higher concentration. **d** Diffusion coefficients of Li^+ and $[TFSI]^-$ at various concentrations. **e** EDL model of Li[TFSI] solution at a lower concentration. **f** EDL model of Li[TFSI] solution at higher concentration. **g** Diffusion coefficients of Li^+ and Cl^- at different temperatures. **h** Diffusion coefficients of Li^+ and $[TFSI]^-$ at different temperatures. **i** The charge transfer amount during contact electrification (CE) between a 10^{-1}M LiCl solution and PTFE at different temperatures. **j** The charge transfer amount during CE between a 10^{-1}M Li[TFSI] solution and PTFE at different temperatures.

hindrance, while Li^+ remained highly mobile. During the CE process, electron transfer rendered the PTFE surface negatively charged, triggering the rapid migration of Li^+ toward the surface to form the OHP of the EDL. The bulky $[TFSI]^-$, unable to enter the Stern layer due to size exclusion, was instead electrostatically adsorbed in the diffuse layer (Fig. 2f). This substantial accumulation of Li^+ near the surface led to charge overcompensation, ultimately reversing the net surface charge from negative to positive.

Temperature critically modulates both CE charge transfer kinetics and ion diffusion behavior[34]. To explore these effects, MD simulations were conducted at different temperatures, focusing on a concentration of 10^{-1} M where charge inversion was experimentally observed. In MD simulations, when the electrolyte was 10^{-1} M LiCl, the diffusion coefficient of Cl^- consistently remained higher than that of Li^+ across the temperature range of 273.15 K to 333.15 K, indicating that temperature-enhanced ionic mobility without altering the relative

diffusion hierarchy (Fig. 2g, S17 and Supplementary Data 9-12). The migration speed of Cl^- consistently exceeded that of Li^+ across all temperatures, and the EDL formation mechanism in 10^{-1} M LiCl remained unchanged. However, when the solution was switched to 10^{-1} M Li[TFSI], a distinct temperature-dependent shift in ion mobility was observed. At 273.15 K and 293.15 K, the diffusion coefficient of $[TFSI]^-$ was lower than that of Li^+, consistent with charge inversion driven by the preferential accumulation of Li^+ at the interface. As the temperature increased to 313.15 K and 333.15 K, the diffusion coefficient of $[TFSI]^-$ surpassed that of Li^+, suggesting a reversal in dominant ionic migration and a potential shift in EDL structure and interfacial charge behavior (Fig. 2h, S18 and Supplementary Data 13-16). To verify the accuracy of the simulation and avoid discrepancies between the real experiment and the simulation, further experiments were conducted to validate the simulation, and triboelectric charge measurement facilities were performed using 10^{-1} M LiCl solutions at varying temperatures. The results revealed a gradual decline in transferred charge with increasing temperature, while the charge polarity remained positive. This suggests that elevated thermal energy weakens interfacial charge transfer without reversing the EDL polarity in relatively symmetric electrolytes. This effect may arise from the enhanced mobility of Li^+ and Cl^- ions at higher temperatures, which accelerates EDL formation and increases charge screening at the interface (Fig. 2i). In the MD simulation, it was found that Li[TFSI] exhibits a diffusion coefficient inversion phenomenon with temperature changes. Therefore, the 10^{-1}M Li[TFSI] solution was selected for further investigation, which exhibited charge reversal in previous experiments. When the experimental temperature was 273.15 K and 293.15 K, the transferred charge was negative, and a charge reversal occurred. However, when the temperature increased to 313.15 K and 333.15 K, the transferred charge reversed to being positive, with no charge reversal observed (Fig. 2j). These findings further validated the proposed model of EDL formation in asymmetric electrolytes and provided additional support for the reliability of using TENG-based triboelectric charge transfer probe for detection across different temperatures.

Upon validation of the simulation accuracy, it was applied to the [EMIM]Cl solution (Figure. S19). For [EMIM]Cl, the overall diffusion coefficient first increased and then decreased, while the diffusion coefficient of Cl^- consistently exceeded that of the bulkier $[EMIM]^+$ at all concentrations. Crucially, this pronounced mobility disparity proved decoupled from charge inversion phenomena, revealing that steric constraints and solvation structure reorganization, rather than simple ion mobility gradients, govern EDL restructuring. This mechanistic disconnect underscores incomplete understanding of asymmetric electrolyte behavior at dielectric interfaces, necessitating further investigation (Figures. S20, S21 and Supplementary Data 17-20). 3D-AFM enabled simultaneous scanning in the XY plane and along the *Z* axis for each X coordinate, allowing the probe to map a volumetric region extending tens of nanometers above the sample surface. By assembling a series of XZ cross-sectional images, a detailed reconstruction of the solid-liquid interfacial architecture becomes possible. To further validate the proposed model for EDL formation in asymmetric electrolytes, 3D-AFM was employed to perform high-resolution nanoscale imaging (Fig. 3a). When the tip approaches the solid-liquid interface, it encounters long-range repulsive or attractive forces from ion distributions in the EDL, resulting in subtle mechanical deflections of the cantilever. These are recorded as force-distance curves and analyzed to extract information about the layering structure. In the experimental setup, the electrolyte solution was confined between a SiO_2 substrate and a top glass surface, with the 3D-AFM cantilever immersed in the electrolyte (Figure. S23). Following CE between the solution and the SiO_2 surface, electron or ion transfer occurred, forming an EDL. This methodological optimization substitutes SiO_2 for characterization due to PTFE's inherent electrostatic interference, which precludes reliable characterization. Nevertheless, PTFE, selected for CE experiments given its superior dielectric constant and electronegativity, yielded consistent charge inversion signatures (Fig. 1 and S22). By scanning the SiO_2 interface, the adsorption profile was visualized, allowing estimation of the Stern layer thickness and direct assessment of the EDL formation model. In the case of LiCl, the thickness of the structured interfacial layer was found to decrease slightly with increasing concentration, although the overall change remained relatively small (Figure. S24). As the electrolyte concentration increased, the EDL became progressively denser, resulting in a slight reduction in the thickness of the Stern layer, consistent with experimental observations. For [EMIM]Cl solutions, a similar trend was observed: the thickness of the interfacial layered structure decreased gradually with increasing concentration, mirroring the behavior observed with LiCl (Figure. S25). To further validate these findings, AFM force-curve scanning was conducted in tapping mode on SiO_2 surfaces exposed to LiCl and [EMIM]Cl solutions of varying concentrations. For each condition, force curves were recorded at ten different points and averaged. The resulting phase and amplitude profiles (Figures. S26, S27) revealed two distinct hydration layers. Similar double-layered hydration structures were observed with LiCl and [EMIM]Cl (Figures. S28, S29). The force curves were converted into force-distance curves using the method of Allard J. Katan[47], revealing oscillatory behavior alternating between attractive and compensatory regions, peaking upon tip–surface contact. To facilitate interpretation, the horizontal axis of the force-distance curves was shifted by subtracting the probe displacement at the point of surface contact, such that the zero point corresponds to the effective probe-surface distance. Notably, the peak-to-peak distance in the LiCl solution remained largely unchanged across different concentrations, consistent with observations from 3D-AFM measurements (Figure. S30). These findings confirmed that the fundamental structure of the EDL in LiCl solutions remained largely invariant across different concentrations, as evidenced by the consistent peak-to-peak distances, in agreement with 3D-AFM measurements. A similar trend was observed in [EMIM]Cl solutions, where the interpeak distance also exhibited minimal variation with increasing concentration (Fig. 3b, S31). However, this similarity is not indicative of experimental insensitivity or limitations but instead reflects a meaningful physical outcome. The AFM technique primarily detects long-range electrostatic, and hydration forces normal to the interface, and is most sensitive to macroscopic features such as the presence, thickness, and layering of the EDL. The consistent force oscillation patterns and interpeak distances across concentrations indicate that the stratified structure of the EDL, comprising the IHP, OHP, and diffuse layer, remains largely intact even at high ionic strength. In other words, concentration variation does not lead to the collapse, merging, or reconstruction of the overall double-layer architecture, but rather preserves its spatial profile. This suggests that the charge reversal phenomenon in [EMIM]Cl did not fundamentally alter the basic structure of the EDL, likely due to the consistent specific adsorption behavior of the same Cl^- anions at the solid interface. The stability of the EDL may be attributed to the overcompensation of surface charge by the adsorbed ions, which preserves the spatial integrity of the IHP and OHP despite variations in ion composition and polarity.

To resolve molecular-scale mechanisms of EDL formation, SERS was employed. Direct interrogation of PTFE-electrolyte interfaces remains precluded by the material's dielectric character and absence of plasmonic activity. To overcome this constraint, we engineered an electrochemically modulated SERS platform using Au nanoparticles (Au-NPs)-modified electrodes under precisely controlled electric fields. This system simulates the interfacial electric field generated by CE without replicating the exact PTFE interface, enabling quantitative

https://doi.org/10.1038/s41467-025-67094-9

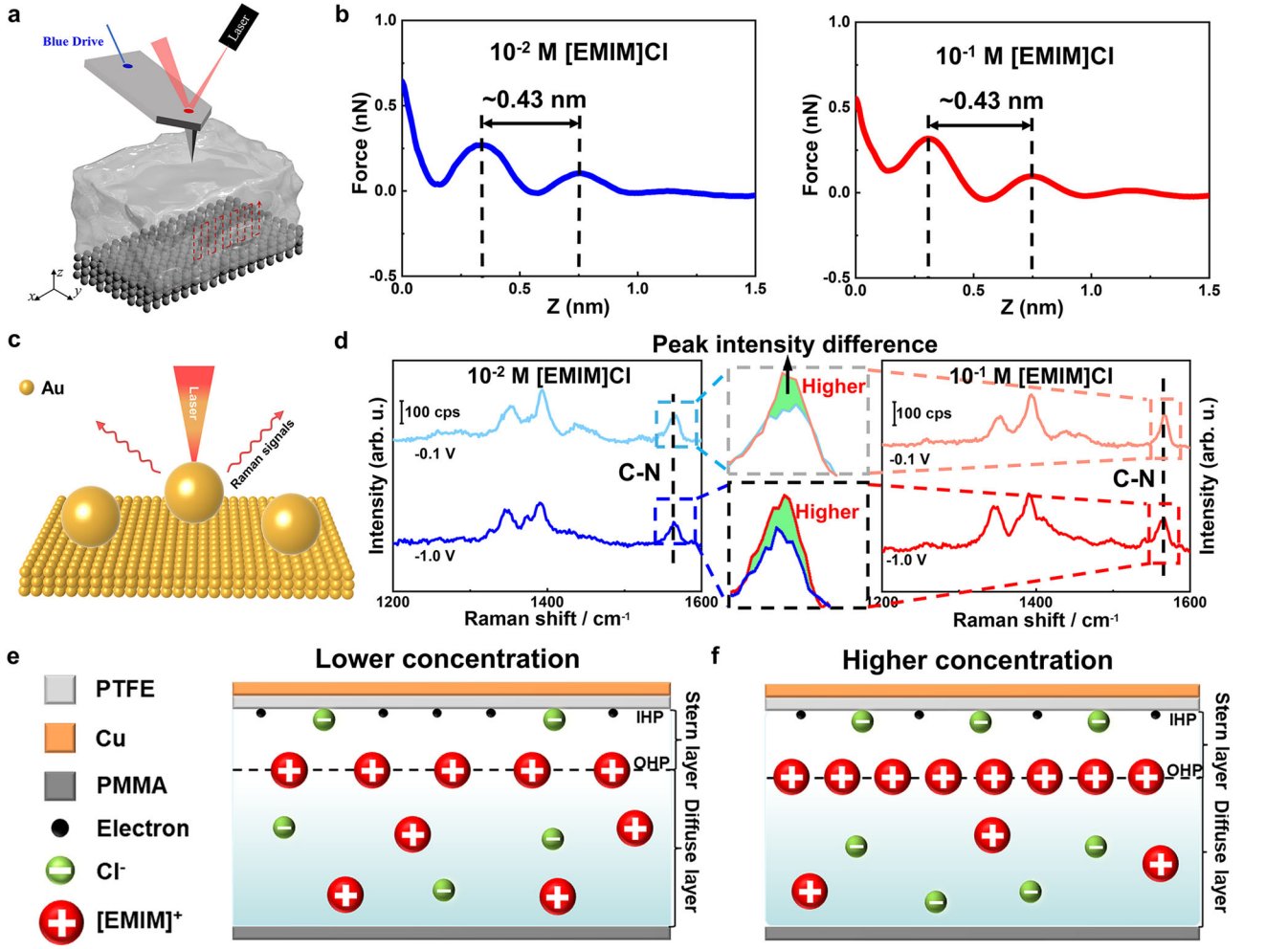

Fig. 3 | Investigation of electrical double layer (EDL) formation in asymmetric electrolytes using 3D-atomic force microscopy (AFM) and surface-enhanced Raman spectroscopy (SERS). a 3D-AFM schematic illustration. **b** Typical hydration force-distance curve in solutions with different concentrations. **c** SERS schematic illustration. **d** Raman signals of [EMIM]Cl solution at different concentrations and potentials. **e** EDL model of [EMIM]Cl solution at a lower concentration. **f** EDL model of [EMIM]Cl solution at higher concentration.

analysis of CE-induced field magnitude and orientation effects on EDL restructuring dynamics. Using ~60 nm Au-NPs modified Au electrode as the plasmonic substrate (Fig. 3c). This approach enabled the identification of species-specific interactions and the structural evolution of the interface under varying conditions. The Au-NPs create strong local electromagnetic fields under laser excitation, enhancing Raman signals from adsorbed molecular species. To emulate the electrostatic environment associated with EDL formation on the dielectrics under triboelectric fields induced by CE, an external electric field was applied via a conventional electrochemical setup, mimicking the interfacial potential generated by CE-driven charge separation. In the experiment, the solution was placed on a flat Au substrate, and then Au-NPs were transferred onto the Au surface, thereby constructing the Au-NPs/solution/Au electrode. Under appropriate laser irradiation, the highly SERS-active Au-NPs generated an extremely strong electromagnetic field, which enhanced the Raman signal of the adsorbed species. According to prior experimental and theoretical studies, solid-liquid CE generates strong localized electric fields at the interface due to charge separation and accumulation during contact or sliding. Reported field strengths can reach 10^8-10^9 V/m[48–50], confined within the EDL region, typically ~1 nm thick under high-concentration electrolytes. To estimate the effective interfacial potential induced by CE, the classical relation is applied:

$$E = \frac{V}{d} \tag{3}$$

where E is the electric field strength, V the electric potential, and d the EDL thickness (~1 nm). Assuming a field strength of 10^9 V/m, the corresponding potential drops across the interface is ~0.1–1 V. Thus, an applied bias of -1 V and -0.1 V in SERS experiments serves as a reasonable approximation of the local electrostatic potential experienced by ions during CE, enabling simulation of field-driven ion arrangements. When the asymmetric electrolyte [EMIM]Cl was used, its Raman response exhibited distinct trends. As shown in Fig. 3d, S32, under an applied negative potential (-1 V), the Raman signal remained largely unchanged between 10^{-3} M and 10^{-2} M. However, at 10^{-1} M, a pronounced increase in the C-N stretching peak at 1565 cm^{-1} was observed, indicating enhanced $[EMIM]^+$ adsorption at the interface. Further increasing the concentration to 1 M produced only minor additional changes, suggesting that the interfacial structure had reached saturation. When the applied potential was adjusted to -0.1 V, the Raman signal remained consistent with that observed at -1 V, with a distinct increase occurring at 10^{-1} M. This enrichment is

attributed to the preferential adsorption and field-driven organization of bulky $[EMIM]^+$ cations in the OHP. Previous studies have suggested that ion hydrophobicity[19] can promote overcompensation, thereby inducing charge reversal. To examine this effect, glass slides were treated with electrolyte solutions of varying concentrations, dried, and subsequently assessed via contact angle measurements using deionized water. With increasing LiCl concentration, the contact angle decreased, indicating enhanced surface hydrophilicity. In contrast, higher concentrations of [EMIM]Cl led to increased contact angles, reflecting a shift toward greater surface hydrophobicity (Figure. S34). Meanwhile, plasma treatment was applied to modify the PTFE surface to enhance its hydrophilicity (Figure. S35). Subsequently, triboelectric charge transfer measurements were conducted using [EMIM]Cl solutions of varying concentrations on both untreated (hydrophobic) and plasma-treated (hydrophilic) PTFE surfaces under otherwise identical conditions. The results revealed a clear distinction: on the untreated PTFE surface, as the [EMIM]Cl concentration increased beyond 10^{-1} M, the transferred charge shifted from negative to positive. In contrast, for the plasma-treated, more hydrophilic surface, although the total charge transfers slightly decreased with increasing electrolyte concentration, no charge polarity reversal was observed across the entire tested concentration range (Figure. S36). These results confirmed that charge reversal occurs when $[EMIM]^+$ exhibits hydrophobic characteristics. As shown in Fig. 3e, at lower concentrations, EDL formation was primarily driven by electron transfer arising from molecular thermal motion at the solid-liquid interface, along with anion adsorption from electrolyte dissociation. This process established the IHP, after which the negatively charged surface attracted large $[EMIM]^+$ cations as counterions to form the OHP, completing the EDL structure. The IHP is predominantly populated by smaller Cl^- anions, while $[EMIM]^+$ cations exist in dilute form within the OHP, resulting in a net negative interfacial charge. In contrast, at higher concentrations (Fig. 3f), $[EMIM]^+$ cations accumulate extensively in the OHP due to enhanced ion-field interactions and possibly hydrophobic self-association, leading to local charge overcompensation and eventual polarity inversion. Li[TFSI] solutions at two representative concentrations (10^{-2} M and 10^{-1} M) were analyzed using the same SERS substrate and experimental setup as for [EMIM]Cl. As shown in the newly added Figure. S33, the Raman spectra exhibit two distinct peaks at ~253 cm^{-1} and 295 cm^{-1}, corresponding to the vibrational mode of Li^+-OH^- complexes and the symmetric/asymmetric stretching of the -CF_3 groups within the $[TFSI]^-$ anion, respectively. Notably, both peaks show significantly increased intensity at 10^{-1} M, indicating enhanced accumulation of Li^+ and $[TFSI]^-$ at the interface with increasing concentration. These spectral changes are consistent with the formation of a more compact and structured EDL under high ionic strength. In particular, the stronger Li^+ signal suggests that, due to its small ionic radius and high charge density, Li^+ is preferentially attracted to the negatively charged PTFE surface generated during CE, facilitating its enrichment at the OHP and promoting the development of a dense EDL. These findings highlight the utility of TENG-based triboelectric charge transfer as a precise and versatile probe for characterizing EDL formation and charge evolution at solid-liquid interfaces.

Formation mechanisms and evolution of EDL in asymmetric electrolyte systems

The formation and evolution of the EDL in asymmetric electrolytes were governed by a sophisticated interplay of multiple physicochemical parameters, including ionic size asymmetry, hydrophobic effects, concentration-dependent behaviors, and ion-ion correlation effects. These collective interactions induced substantial deviations from classical EDL theories, particularly in high-concentration electrolyte systems (>10^{-1} M), where conventional mean-field approximations frequently failed to accurately capture the observed interfacial phenomena. Through a combination of experimental observations and computational analyses, distinct mechanisms responsible for EDL formation across various electrolyte systems were identified, especially under high-concentration (exceeding 10^{-1}M) conditions. By integrating classical EDL theory with triboelectric frameworks, we establish models resolving interfacial charge dynamics across diverse solid-liquid interfaces, including high ionic strength regimes. It confirms material-agnostic applicability. This model integrates the experimental observations into a form adapted for dielectric interfaces, providing a coherent explanation of the charge inversion and structural transitions revealed in the study. This paradigm simultaneously advances fundamental EDL mechanisms and enables programmable charge manipulation for next-generation iontronic power, sensing, and neuromorphic devices. When the solution used was a symmetric electrolyte, such as LiCl, it dissociated in water into Li^+ and Cl^- ions, thereby increasing the number of available free ions in the system. As shown in Fig. 4a, the ions in the LiCl solution (particularly Cl^- and Li^+) actively participated in the formation of the EDL at the solid-liquid interface. Specifically, when the solution encountered the solid surface, Cl^- ions and the electrons generated during the CE process jointly contributed to the formation of the IHP. Due to its small size, high mobility, and specific adsorption capability, the Cl^- was able to rapidly adsorb onto the solid surface, forming the foundation of the IHP together with the initially transferred electrons. Meanwhile, due to the high hydration-free energy of Li^+, it typically could not escape from its hydration shell to enter the dipole layer of water molecules and thus could not directly enter the IHP. As a result, the hydrated Li^+ ions formed the OHP. Together, these layers constituted the Stern layer which, along with the diffuse layer, formed the complete EDL structure. As the concentration increased and exceeded a critical threshold (10^{-1} M), the number of ions in the solution rose significantly, and the Coulombic interactions between ions became substantially stronger, driving the formation of a more compact EDL, as illustrated in Fig. 4b. When an asymmetric electrolyte solution with large-sized anions, such as Li[TFSI] was used, the electrolyte dissociated in the solution, releasing small-sized Li^+ and large-sized $[TFSI]^-$. Under low-concentration conditions (< 10^{-1} M), when the solution encountered a solid surface, the IHP was rapidly formed[2] (Fig. 4c). Meanwhile, Li^+ as counterions migrated to the solid surface under the action of electrostatic attraction, forming the OHP and thereby completing the formation of the EDL. However, when the solution concentration increased above 10^{-1} M, the diffusion speed of $[TFSI]^-$ significantly decreased and became lower than that of Li^+. Under these conditions, the electrons initially transferred during the CE process, together with the specifically adsorbed ions, rapidly formed the IHP. Then, many Li^+ ions were quickly adsorbed onto the negatively charged solid surface, forming a dense OHP, which might prevent the more slowly diffusing $[TFSI]^-$ anions from entering the Stern layer, ultimately completing the construction of the EDL (Fig. 4d). When an asymmetric electrolyte solution with large-sized cations, such as [EMIM]Cl, was used, the solution dissociated into large-sized $[EMIM]^+$ and small-sized Cl^-. Under low-concentration conditions (< 10^{-1} M), when the solution encountered a solid surface, the electrons initially transferred during the CE process, together with Cl^-, rapidly formed the IHP (Fig. 4e). Meanwhile, $[EMIM]^+$ as counterions, migrated to the solid surface under the action of electrostatic attraction, forming the OHP and thereby completing the initial construction of the EDL. However, when the solution concentration increased above 10^{-1} M, the IHP was still composed of electrons and Cl^-. Due to changes in molecular conformation, enhanced interfacial interactions, and the hydrophobic nature of $[EMIM]^+$, $[EMIM]^+$ exhibited a stronger tendency to absorb onto the solid surface, leading to over-absorption during the formation of the OHP, the positive charge density of the OHP significantly increased, forming a diffuse layer with a net negative charge (Fig. 4f). Through TENG-based triboelectric charge transfer measurements, a

https://doi.org/10.1038/s41467-025-67094-9

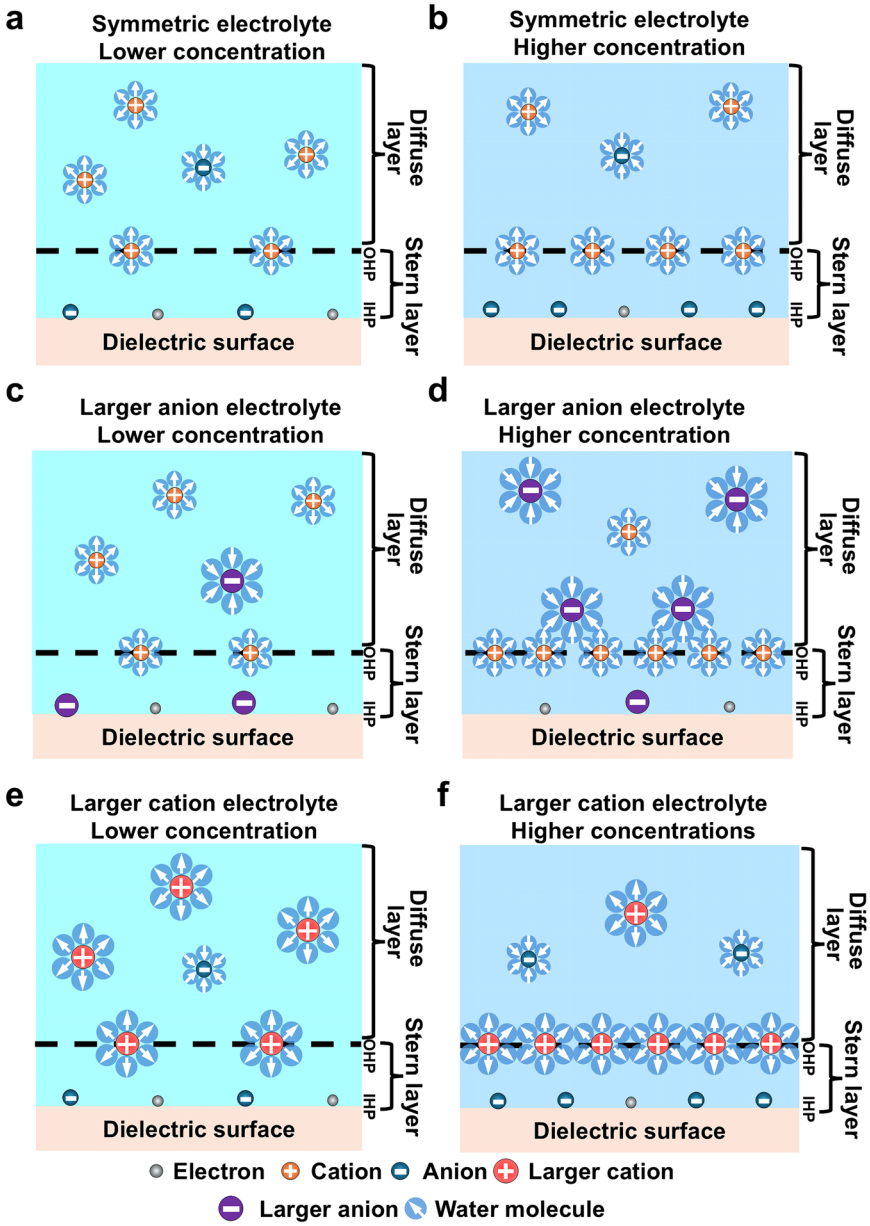

Fig. 4 | Electrical double layer (EDL) models for different electrolytes. a EDL model formed at lower concentrations in a symmetric electrolyte solution. (inner Helmholtz plane (IHP), outer Helmholtz plane (OHP)) **b** EDL model formed at higher concentrations in a symmetric electrolyte solution. **c** EDL model formed at lower concentrations in a larger anion electrolyte solution. **d** EDL model formed at higher concentrations in a larger anion electrolyte solution. **e** EDL model formed at lower concentrations in a larger cation electrolyte solution. **f** EDL model formed at higher concentrations in a larger cation electrolyte solution.

multifunctional and straightforward EDL characterization method has been developed that surpasses traditional approaches. Corresponding EDL theoretical models were proposed by combining classical models with the characteristics of different electrolytes, enabling the elucidation of interfacial charge distribution and the mechanisms underlying EDL formation. This work advances the fundamental understanding of charge regulation at dielectric interfaces and paves the way for the application of iontronics in energy storage and intelligent sensing technologies.

Discussion

In this study, a triboelectric charge transfer approach utilizing a TENG is presented as a straightforward probe for operando monitoring of the EDL at solid-liquid interfaces of non-conductive materials across diverse electrolytes. A fundamental experimental gap was resolved by introducing the cost-effective and operando methodology to probe EDLs at dielectric interfaces. Conventional techniques (e.g., KPFM, electrochemical impedance) are fundamentally constrained at dielectric interfaces by conductivity requirements, charge-trapping artifacts, and field-perturbation effects on EDL structures. Our triboelectric charge transfer probe leverages CE as an intrinsic charge-transfer metric, enabling zero-bias, electrode-free interrogation of EDL, unlocking previously inaccessible dielectric interfaces. In addition, it confirms material-agnostic applicability to resolve interfacial charge dynamics across diverse solid-liquid interfaces, including high ionic strength regimes. This paradigm simultaneously advances fundamental EDL mechanisms and enables programmable charge manipulation for next-generation iontronic power, sensing, and neuromorphic devices. By reconciling previously conflicting models through a unified structural framework of EDL reorganization, these

findings redefine the EDL as a tunable functional platform for iontronic device engineering.

Methods

Materials

The 50 μm-thick Polytetrafluoroethylene (PTFE) film (industrial grade) was purchased from Aladdin, while the 5 mm-thick Polymethyl methacrylate (PMMA) film (industrial grade) was acquired from Alibaba. The DI water with a resistivity of 18.2 MΩ·cm used here was produced by a deionizer (HHitech, China). Lithium chloride (LiCl) (≥99%) was purchased from Aladdin, Lithium bis(trifluoromethanesulphonyl)imide (Li[TFSI]) (≥99%) was purchased from Aladdin, and 1-Ethyl-3-methylimidazolium Chloride([EMIM]Cl) (98%) was purchased from Aladdin litmus reagent (1% ± 0.05%). Furthermore, all the chemical reagents used in this experiment are of analytical grade and require no further treatment.

Characterization and Measurement

TENG-based triboelectric charge measurement experiment: The electrical output performance of the triboelectric charge, including transferred charge, was tested using a programmable electrometer (Keithley 6514). Real-time data collection was achieved through a software platform built based on LabVIEW. The vertical uniaxial motor (Linmot HC14-10) was used to apply a variable vertical force. The Faraday cylinder was used to test the charge carried by the droplets sliding through the tested film.

KPFM Experiments: The experiment was conducted using a commercial AFM device, Multimode 8 (Bruker, USA). A conductive tip (Oxford AC240TM-R3) was used as the probe.

3D-AFM Experiment: Scanning was performed in liquid using a Cypher ES system with environmental control (Asylum Research, Oxford Instruments). The cantilever oscillation was driven by the BlueDrive module. The probe (Arrow UHF Ultra High Frequency–Reflex coating) had a resonance frequency of ~700–2000 kHz. Morphological images were collected at a scan rate of 10~15 Hz with a resolution of 256 × 256 lines. For XZ images, the total X displacement consisted of 256 data points.

Raman spectra: Raman spectra (100–4000 cm^{-1}) were acquired using a Horiba XploRA confocal Raman microscope equipped with a 638 nm laser at 1% power for 30 s. A 50× objective lens with a numerical aperture (NA) of 0.5 was used for signal collection.

Simulations methods

MD simulations were performed using the LAMMPS package (29 Aug 2024 version). The general Amber force field (GAFF) was applied to describe the $[TFSI]^-$ anion, while the parameters for Li^+ were obtained from the optimized potentials for liquid simulations (OPLS) field. Water molecules were modeled using the SPC/fw water model, and the $[EMIM]^+$ cation was represented using the all-atom optimized potentials for liquid simulations (OPLS-AA) field (Tables S2, S3 and S4). Long-range electrostatic interactions were calculated using the particle-particle particle-mesh (PPPM) method, with a cutoff distance of 12 Å applied for non-bonded interactions. A partial charge scaling approach is employed, with the charge reduced from ± 1e to ± 0.8e, to indirectly account for polarization effects, thereby enhancing the consistency between structural and diffusion simulations.

Each simulation box was equilibrated for 2 ns in the isothermal-isobaric (NPT) ensemble to determine the density, followed by an 8 ns production run in the canonical ensemble (NVT). The pressure was maintained at 1 atm during all constant pressure simulations, facilitating isotropic volume fluctuations. To ensure stability in bond lengths and angles of the water molecules, the SHAKE algorithm was applied. Temperature control was achieved using a Nose-Hoover thermostat set to 293 K, with a time step of 1 fs.

Data availability

The authors declare that all the data that support the findings of this study are available within the article and its supplementary information files. Source data are provided with this paper.

References

1. Greco, A. et al. Ultrafast aqueous electric double layer dynamics. *Science* **388**, 405–410 (2025).
2. Zhou, Y. et al. Real-time mass spectrometric characterization of the solid–electrolyte interphase of a lithium-ion battery. *Nat. Nanotechnol.* **15**, 224–230 (2020).
3. Yang, L. et al. A moisture-enabled fully printable power source inspired by electric eels. *Proc. Natl. Acad. Sci. USA.* **118**, e2023164118 (2021).
4. Liu, J. et al. Nonaqueous contact-electro-chemistry via triboelectric charge. *J. Am. Chem. Soc.* **146**, 31574–31584 (2024).
5. Lin, S., Chen, X. & Wang, Z. L. Contact electrification at the liquid–solid interface. *Chem. Rev.* **122**, 5209–5232 (2022).
6. Wu, Q., McDowell, M. T. & Qi, Y. Effect of the electric double layer (EDL) in multicomponent electrolyte reduction and solid electrolyte interphase (SEI) formation in lithium batteries. *J. Am. Chem. Soc.* **145**, 2473–2484 (2023).
7. Yuan, X. et al. Engineering battery corrosion films by tuning electrical double layer composition. *Joule* **8**, 3038–3053 (2024).
8. Du, Y. et al. Multi-receptor skin with highly sensitive tele-perception somatosensory. *Sci. Adv.* **10**, eadp8681 (2024).
9. Helmholtz, H. Ueber einige Gesetze der Vertheilung elektrischer Ströme in körperlichen Leitern mit Anwendung auf die thierisch-elektrischen Versuche. *Ann. der Phys.* **165**, 211–233 (1853).
10. Chapman, D. L. LI. A contribution to the theory of electrocapillarity. *Phys. Phil.* **25**, 475–481 (1913).
11. Grahame, D. C. The electrical double layer and the theory of electrocapillarity. *Chem. Rev.* **41**, 441–501 (1947).
12. Lin, S., Xu, L., Chi Wang, A. & Wang, Z. L. Quantifying electron-transfer in liquid-solid contact electrification and the formation of electric double-layer. *Nat. Commun.* **11**, 399 (2020).
13. Nie, J. et al. Probing contact-electrification-induced electron and ion transfers at a liquid–solid interface. *Adv. Mater.* **32**, 1905696 (2020).
14. Fedorov, M. V. & Kornyshev, A. A. Ionic liquids at electrified interfaces. *Chem. Rev.* **114**, 2978–3036 (2014).
15. Merlet, C. et al. Highly confined ions store charge more efficiently in supercapacitors. *Nat. Commun.* **4**, 2701 (2013).
16. Esfandiar, A. et al. Size effect in ion transport through angstrom-scale slits. *Science* **358**, 511–513 (2017).
17. Calero, C., Faraudo, J. & Bastos-González, D. Interaction of monovalent ions with hydrophobic and hydrophilic colloids: charge inversion and ionic specificity. *J. Am. Chem. Soc.* **133**, 15025–15035 (2011).
18. Martín-Molina, A., Rodríguez-Beas, C. & Faraudo, J. Charge reversal in anionic liposomes: experimental demonstration and molecular origin. *Phys. Rev. Lett.* **104**, 168103 (2010).
19. He, X. et al. Chaotropic monovalent anion-induced rectification inversion at nanopipettes modified by polyimidazolium brushes. *Angew. Chem. Int. Ed. Engl.* **57**, 4590–4593 (2018).
20. Andersson, L., Sprik, M., Hutter, J. & Zhang, C. Electronic response and charge inversion at polarized gold electrode. *Angew. Chem. Int. Ed.* **64**, e202413614 (2025).
21. Lin, K. et al. Charge inversion and calcium gating in mixtures of ions in nanopores. *J. Am. Chem. Soc.* **142**, 2925–2934 (2020).
22. Parsons, R. The electrical double layer: recent experimental and theoretical developments. *Chem. Rev.* **90**, 813–826 (1990).
23. Grahame, D. C. & Parsons, R. Components of charge and potential in the inner region of the electrical double layer: aqueous

potassium chloride solutions in contact with mercury at 25. *J. Am. Chem. Soc.* **83**, 1291–1296 (1961).
24. Li, C.-Y. et al. In situ probing electrified interfacial water structures at atomically flat surfaces. *Nat. Mater.* **18**, 697–701 (2019).
25. Gu, Y. et al. Resolving nanostructure and chemistry of solid-electrolyte interphase on lithium anodes by depth-sensitive plasmon-enhanced Raman spectroscopy. *Nat. Commun.* **14**, 3536 (2023).
26. Yin, X.-T. et al. Unraveling the energy storage mechanism in graphene-based nonaqueous electrochemical capacitors by gap-enhanced Raman spectroscopy. *Nat. Commun.* **15**, 5624 (2024).
27. Gonella, G. et al. Water at charged interfaces. *Nat. Rev. Chem.* **5**, 466–485 (2021).
28. Zhong, Y.-X. et al. Resolving fine structures of the electric double layer of electrochemical interfaces in ionic liquids with an afm tip modification strategy. *J. Am. Chem. Soc.* **136**, 14682–14685 (2014).
29. Tsai, W.-Y., Taberna, P.-L. & Simon, P. Electrochemical quartz crystal microbalance (EQCM) study of ion dynamics in nanoporous carbons. *J. Am. Chem. Soc.* **136**, 8722–8728 (2014).
30. Bedzyk, M. J., Bommarito, G. M., Caffrey, M. & Penner, T. L. Diffuse-double layer at a membrane-aqueous interface measured with x-ray standing waves. *Science* **248**, 52–56 (1990).
31. Terris, B. D., Stern, J. E., Rugar, D. & Mamin, H. J. Contact electrification using force microscopy. *Phys. Rev. Lett.* **63**, 2669–2672 (1989).
32. Sobarzo, J. C. et al. Spontaneous ordering of identical materials into a triboelectric series. *Nature* **638**, 664–669 (2025).
33. Shi, L. et al. Water structure and electric fields at the interface of oil droplets. *Nature* **640**, 87–93 (2025).
34. Wei, Y. et al. Contact electrification at the solid–liquid transition interface. *Mater. Today* **74**, 2–11 (2024).
35. Li, X. et al. Harnessing triboiontronic Maxwell's demon by triboelectric-induced polarization for efficient energy-information flow. *Joule* **9**, 101888 (2025).
36. Zhang, J., Lin, S., Zheng, M. & Wang, Z. L. Triboelectric nanogenerator as a probe for measuring the charge transfer between liquid and solid surfaces. *ACS Nano* **15**, 14830–14837 (2021).
37. Zhang, J. et al. Triboelectric nanogenerators as a probe for studying charge transfer at liquid–solid interface. *MRS Bull.* **50**, 327–335 (2025).
38. Zhang, J., Lin, S. & Wang, Z. L. Triboelectric nanogenerator array as a probe for in situ dynamic mapping of interface charge transfer at a liquid–solid contacting. *ACS Nano* **17**, 1646–1652 (2023).
39. Zhang, J. et al. Triboelectric Spectroscopy for In Situ Chemical Analysis of Liquids. *J. Am. Chem. Soc.* **146**, 6125–6133 (2024).
40. Li, R. et al. Probing Leidenfrost effect via contact electrification. *Nano Energy* **134**, 110570 (2025).
41. Li, X., Wang, Z. L. & Wei, D. Scavenging energy and information through dynamically regulating the electrical double layer. *Adv. Funct. Mater.* **34**, 2405520 (2024).
42. Li, X. et al. Triboiontronics for efficient energy and information flow. *Matter* **6**, 3912–3926 (2023).
43. Li, X. et al. Triboiontronics with temporal control of electrical double layer formation. *Nat. Commun.* **15**, 6182 (2024).
44. Xiong, T. et al. Neuromorphic functions with a polyelectrolyte-confined fluidic memristor. *Science* **379**, 156–161 (2023).
45. He, X. et al. Micrometer-scale ion current rectification at polyelectrolyte brush-modified micropipets. *J. Am. Chem. Soc.* **139**, 1396–1399 (2017).
46. France-Lanord, A. & Grossman, J. C. Correlations from Ion Pairing and the Nernst-Einstein Equation. *Phys. Rev. Lett.* **122**, 136001 (2019).
47. Li, H. et al. Evolution of interfacial hydration structure induced by ion condensation and correlation effects. *Angew. Chem. Int. Ed.* **64**, e202418029 (2025).
48. Kathmann, S. M., Kuo, I. F. W. & Mundy, C. J. Electronic effects on the surface potential at the vapor–liquid interface of Water. *J. Am. Chem. Soc.* **130**, 16556–16561 (2008).
49. Hao, H., Leven, I. & Head-Gordon, T. Can electric fields drive chemistry for an aqueous microdroplet?. *Nat. Commun.* **13**, 280 (2022).
50. Xiong, H., Lee, J. K., Zare, R. N. & Min, W. Strong electric field observed at the interface of aqueous microdroplets. *J. Phys. Chem. Lett.* **11**, 7423–7428 (2020).

Acknowledgements

This work is supported by the National Natural Science Foundation of China (Grant No. 22479016 D.W.).

Author contributions

D.W. and Z.L.W. proposed the idea and the project. D.W. designed all the experiments and supervised the whole project. Y.W., X.L., Y.G., and L.D. carried out the experiments in this paper and analyzed the corresponding data. Y.W. and X.L. analyzed the operation principle of TENG. X.G. and Z.Q.Z. performed molecular dynamics simulations and conducted the analysis. C.K., J.B., and A.I. performed and analyzed the Raman experiments. Y.G., L.D., and Z.Q.T. performed and analyzed the SERS experiments. All the authors discussed the results and commented on the manuscript. D.W. and W.Y. wrote this paper.

Competing interests

The authors declare no competing interests.

Additional information

Supplementary information The online version contains supplementary material available at https://doi.org/10.1038/s41467-025-67094-9.

Correspondence and requests for materials should be addressed to Zhong-Qun Tian, Zhong Lin Wang or Di Wei.

Peer review information *Nature Communications* thanks Chang Hyuck Choi, Bin Kang and the other, anonymous, reviewer(s) for their contribution to the peer review of this work. A peer review file is available.

Yu Wei[1,2,8], Xiang Li[1,2,8], Yu Gu[3,8], Lian Ding[3], Xiang Gao[4], Zhongqiang Zhang[4], Carita Kvarnström[5], Johan Bobacka[6], Ari Ivaska[6], Zhong-Qun Tian[3] ✉, Zhong Lin Wang[1] ✉ & Di Wei[1,7] ✉

[1]Beijing Institute of Nanoenergy and Nanosystems, Chinese Academy of Sciences, Beijing, P. R. China. [2]School of Nanoscience and Engineering, University of Chinese Academy of Sciences, Beijing, P. R. China. [3]School of Electronic Science and Engineering, State Key Laboratory of Physical Chemistry of Solid Surfaces, College of Chemistry and Chemical Engineering, IKKEM, Xiamen University, Xiamen, China. [4]School of Mechanical Engineering, Jiangsu University, Zhenjiang, P. R. China. [5]Department of Chemistry, University of Turku, Henrikinkatu 2, 20014 Turku, Finland. [6]Laboratory of Molecular Science and Engineering, Åbo Akademi University, Henriksgatan 2, 20500 Turku, Finland. [7]Centre for Photonic Devices and Sensors, University of Cambridge, 9 JJ Thomson Avenue, Cambridge, UK. [8]These authors contributed equally: Yu Wei, Xiang Li, Yu Gu. ✉e-mail: zqtian@xmu.edu.cn; zlwang@binn.cas.cn; weidi@binn.cas.cn